Available online at www.sciencedirect.com
ScienceDirect
Trans. Nonferrous Met. Soc. China 35(2025) 1742−1757
Transactions of Nonferrous Metals Society of China
www.tnmsc.cn

Microstructure, phase stability, and mechanical properties of Al−Li−Mg−Ti−M (M=Zn, Zr, V) lightweight high-entropy alloys

Quan DONG[1], Meng LI[1], Yu-fei ZHANG[1], Jing ZHANG[1,2]

1. College of Materials Science and Engineering, Chongqing University, Chongqing 400044, China;
2. National Engineering Research Center for Magnesium Alloys, Chongqing University, Chongqing 400044, China

Received 7 October 2023; accepted 30 June 2024

Abstract: The microstructural evolution, phase stability, and mechanical properties of Al−Li−Mg−Ti−M (M=Zn, Zr, V) lightweight high-entropy alloys (LW-HEAs) were investigated. The LW-HEAs with three components, $Al_{20}Li_{20}Mg_{10}Ti_{40}Zn_{10}$ (#Zn), $Al_{20}Li_{20}Mg_{10}Ti_{30}Zr_{20}$ (#Zr), and $Al_{20}Li_{20}Mg_{10}Ti_{30}V_{20}$ (#V), were designed according to the thermodynamic design criteria of HEA, and prepared via a combination process of mechanical alloying and cold-press sintering. The effects of alloy composition and sintering temperature on the microstructure and mechanical properties of the LW-HEAs were studied. The results show that the as-milled Al−Li−Mg−Ti−M (M=Zn, Zr, V) LW-HEAs form a simple structure with HCP-type solid solution as the primary phase, a dual-HCP type solid solution phase, and a BCC phase, respectively. After cold-press sintering, the #Zn and #V alloys undergo obvious phase transformation; while the #Zr alloy with dual-HCP phases exhibits the best phase stability during heat treatment. The #V-750 °C alloy demonstrates the maximum hardness and specific strength of HV 595.2 and 625 MPa·cm^3/g, respectively, under the combined effect of solid solution strengthening of BCC phase and precipitation strengthening of β-$AlTi_3$. Moreover, the #Zr-650 °C, #Zr-750 °C, and #Zn-650 °C alloys are expected to have excellent plasticity.

Key words: lightweight high-entropy alloy; mechanical alloying; microstructural evolution; phase stability; specific strength; plasticity

1 Introduction

Unlike traditional alloys with only one or two main components, high-entropy alloys (HEAs) are composed of various main components with equimolar/near-equimolar ratios and unexpectedly have simple phase structures. HEAs exhibit more excellent properties than traditional alloys, such as high strength [1,2], high hardness [3,4], high wear resistance [5,6], and high corrosion resistance [7,8]. However, most of the reported HEAs are composed of transition group elements, and the density of the majority alloys exceeds 6 g/cm^3 [9]. Designing and preparing new lightweight alloys with both low density and excellent performance become a research hotspot in high entropy alloy.

Introducing light elements, especially Mg, Li, Al, and Ti, etc., into the compositional design can significantly reduce the density of HEAs [10−14]. For example, MITRICĂ et al [10] designed a series of Al−Cu−Si−Zn−Mg light weight HEAs (LW-HEAs) with a density lower than 3.57 g/cm^3, and the alloy density decreased with the increase of Al and Mg contents. The alloy phases include a FCC phase, Mg_2Si phase, and Al_2Cu phase. JI et al [11] prepared $Al_{35}Mg_{30-x}Zn_{30}Cu_5Si_x$ LW-HEAs with a density of 3.71−3.78 g/cm^3, and the phase constitute included FCC phase, Si phase, Mg_2Si phase, and Mg−Al−Zn phase. JIA et al [13] designed a series of Al−Li−Mg−Si−Ca−(Y) LW-HEAs with a density lower than 1.57 g/cm^3, and the phases of these alloys

Corresponding author: Jing ZHANG, Tel: +86-23-65111167, E-mail: jingzhang@cqu.edu.cn
https://doi.org/10.1016/S1003-6326(25)66780-X

consisted of HCP and/or BCC, and other two or more intermetallics.

Based on the LW-HEAs reported above, it can be summarized that in addition to Al and/or Ti elements, the alloys contain at least one other light element that is easy to be immiscible with transition metal elements or to form various intermetallics, such as Si, alkali metal, and alkaline-earth metal elements. As a result, multi-phase structure instead of a single-phase structure is inevitably formed. Moreover, even if a single-phase structure is obtained through mechanical alloying, many intermetallics will be precipitated during the subsequent sintering or heat treatment [4,12,15]. Obviously, the single-phase-structured LW-HEAs exhibit poor thermal stability. Encouragingly, YOUSSEF et al [14] designed and prepared an $Al_{20}Li_{20}Mg_{10}Sc_{20}Ti_{30}$ LW-HEA with a density of 2.67 g/cm^3 via mechanical alloying. Although the phase structure transformed from single-phase FCC to HCP after annealing at 500 °C, no intermetallics were formed. Further, DONG et al [4] prepared a series of $(AlLiMg_{0.5}Ti_{1.5})_{100-x}Sc_x$ LW-HEAs via a combination method of mechanical alloying and cold-press sintering, and found that the addition of Sc improved alloy phase stability and inhibited phase transformation during the sintering. It is therefore inspiring to explore more LW-HEAs with high phase stability, aiming to figure out the inherent rule of phase formation and transformation for LW-HEAs.

In this work, AlLiMgTi-based LW-HEAs with different fifth components were designed using empirical parameter criteria of HEAs. Three LW-HEAs, $Al_{20}Li_{20}Mg_{10}Ti_{40}Zn_{10}$, $Al_{20}Li_{20}Mg_{10}Ti_{30}Zr_{20}$, and $Al_{20}Li_{20}Mg_{10}Ti_{30}V_{20}$, which meet the design requirements, were prepared via a combination process of mechanical alloying and cold-press sintering. The effects of elements and sintering temperature on the microstructure and properties of Al−Li−Mg−Ti−M LW-HEAs were discussed. This work hopefully provides valuable data and fundamental knowledge for the design of thermal stable LW-HEAs.

2 Experimental

2.1 Alloy design

To meet the requirements of lightweight, low-density elements, Al, Li, Mg, and Ti, were selected as the mandatory components of the alloys. Si, Ca, V, Cr, Fe, Co, Ni, Cu, Zn, Y, Zr, and Nb elements were selected as the fifth component (denoted as M), and the characteristic parameters of these elements are shown in Table 1 [16].

Table 1 Characteristic parameters of elements in Al−Li−Mg−Ti−M LW-HEAs [16]

Element	Structure at RT	Density/ (g·cm^{-3})	Atom radius/ pm	T_m/ K	Pauling EN	VEC
Li	A2 (BCC)	0.53	151.94	454	0.98	1
Mg	A3 (HCP)	1.74	160.13	923	1.31	2
Al	A1 (FCC)	2.70	143.17	933	1.61	3
Ti	A3 (HCP)	4.50	146.15	1941	1.54	4
Si	A4 (Cubic)	2.33	115.30	1687	1.90	4
Ca	A1 (FCC)	1.53	197.60	1115	1.00	2
V	A2 (BCC)	6.12	131.60	2183	1.63	5
Cr	A2 (BCC)	7.19	124.91	2180	1.66	6
Fe	A2 (BCC)	7.88	124.12	1811	1.83	8
Co	A3 (HCP)	8.84	125.10	1768	1.88	9
Ni	Al (FCC)	8.91	124.59	1728	1.91	10
Cu	Al (FCC)	8.94	127.8	1358	1.90	11
Zn	A3 (HCP)	7.14	139.45	693	1.95	12
Y	A3 (HCP)	4.47	180.15	1975	1.22	3
Zr	A3 (HCP)	6.51	160.25	2128	1.33	4
Nb	A2 (BCC)	8.58	142.90	2750	1.60	5
Mo	A2 (BCC)	10.23	136.26	2896	2.16	6

T_m is melting point; Pauling EN represents Pauling electronegativity; VEC is valence electron concentration

Based on the composition of $Al_{20}Li_{20}Mg_{10}Sc_{20}Ti_{30}$ LW-HEA [4,14], a series of HEAs with the atomic ratio of $Al_{20}Li_{20}Mg_{10}Ti_{30}M_{20}$ (M= Si, Ca, V, Cr, Fe, Co, Ni, Cu, Zn, Y, Zr, and Nb) were designed. According to the design criteria of HEAs [17,18], the thermodynamic and physical parameters of $Al_{20}Li_{20}Mg_{10}Ti_{30}M_{20}$ alloys were calculated, including atomic size difference (δ), mixing enthalpy change (ΔH_{mix}), mixing entropy change (ΔS_{mix}), entropy−enthalpy ratio (Ω), valence electron concentration (VEC), electronegativity difference ($\Delta\chi$), and melting point (T_m):

$$\delta=\sqrt{\sum_{i=1}^{n}c_i\left(1-r_i\Big/\sum_{i=1}^{n}c_ir_i\right)^2}\times100\% \quad (1)$$

$$\Delta H_{\mathrm{mix}}=\sum_{i=1,i\neq j}^{n}4\Delta H_{\mathrm{AB}}^{\mathrm{mix}}c_i c_j \tag{2}$$

$$\Delta S_{\mathrm{mix}}=-R\sum_{i=1}^{n}c_i\ln c_i \tag{3}$$

$$\Omega=\frac{T_{\mathrm{m}}\Delta S_{\mathrm{mix}}}{|\Delta H_{\mathrm{mix}}|} \tag{4}$$

$$T_{\mathrm{m}}=\sum_{i=1}^{n}c_i(T_{\mathrm{m}})_i \tag{5}$$

$$\mathrm{VEC}=\sum_{i=1}^{n}c_i(\mathrm{VEC})_i \tag{6}$$

$$\Delta\chi=\sqrt{\sum_{i=1}^{n}c_i\left(\chi_i-\sum_{i=1}^{n}c_i\chi_i\right)^2} \tag{7}$$

where c_i and c_j are the molar fractions of the ith and jth components, respectively, r_i is the radius of the ith atom, n is the number of components, $\Delta H_{\mathrm{AB}}^{\mathrm{mix}}$ is the mixing enthalpy change between elements A and B (the data are taken from Table 2 [19]), R is the molar gas constant (R=8.314 J/(mol·K)), $(\mathrm{VEC})_i$ is the valence electron concentration of the ith component, and χ_i is the Pauling electronegativity of the ith component. Figure 1 shows the thermodynamic parameters of the $Al_{20}Li_{20}Mg_{10}Ti_{30}M_{20}$ alloys. According to the design requirements of HEA [20]: $\delta<6.6\%$, $-15\ \mathrm{kJ/mol}<\Delta H_{\mathrm{mix}}<10\ \mathrm{kJ/mol}$, and $\Omega>1.1$, three alloys, $Al_{20}Li_{20}Mg_{10}Ti_{30}V_{20}$ (named #V), $Al_{20}Li_{20}Mg_{10}Ti_{30}Zr_{20}$ (named #Zr), and $Al_{20}Li_{20}Mg_{10}Ti_{30}Zn_{20}$, were screened to meet the design requirements. Considering the low melting point of Zn element, higher Zn content leads to lower melting point, thus the Zn content in $Al_{20}Li_{20}Mg_{10}Ti_{30}Zn_{20}$ alloy is adjusted and alloy $Al_{20}Li_{20}Mg_{10}Ti_{40}Zn_{10}$ (named #Zn) that still meets the design requirements of HEA is determined. The theoretical density (ρ_{theor}) of the alloy can be calculated by the following formula [21]:

$$\rho_{\mathrm{theor}}=\sum_{i=1}^{n}c_i A_i\Big/\sum_{i=1}^{n}(c_i A_i/\rho_i) \tag{8}$$

where A_i and ρ_i are the atomic mass and density of the ith component, respectively. The calculated ρ_{theor} values of the #Zn, #Zr, and #V alloys are 3.13, 3.48, and 3.11 g/cm^3, respectively. Obviously, the alloys

Table 2 Mixing enthalpy changes between elements in Al−Li−Mg−Ti−M (M=Zn, Zr, V) LW-HEAs [19]

Element	$\Delta H_{\mathrm{AB}}^{\mathrm{mix}}$/(kJ·mol^{-1})			
	Al	Li	Mg	Ti
Al	−			
Li	−4	−		
Mg	−2	0	−	
Ti	−30	34	16	−
Zn	1	−7	−4	8
Zr	−44	27	6	0
V	−16	37	23	−2

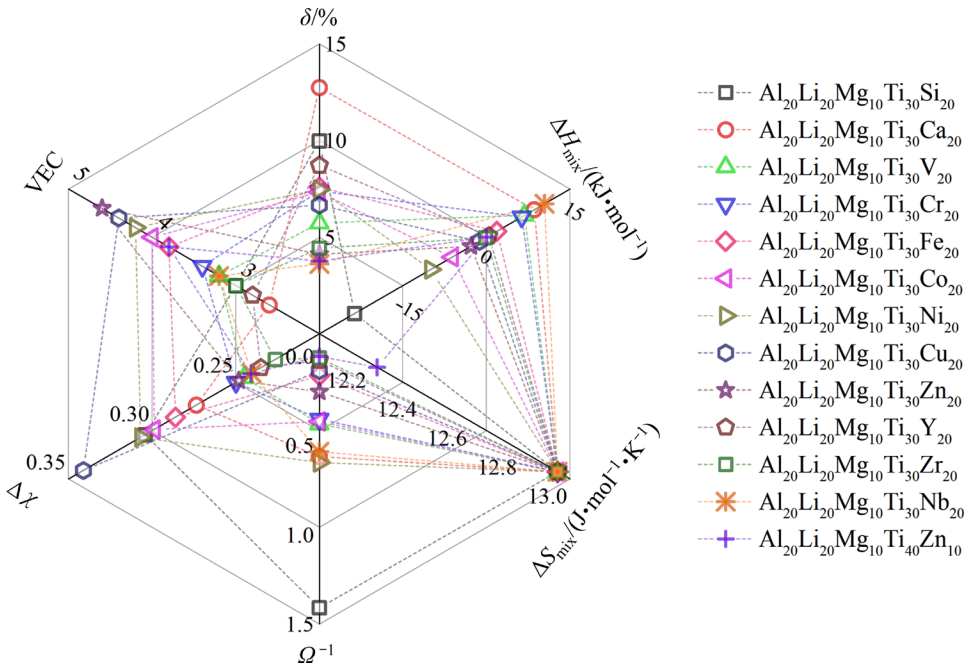

Fig. 1 Thermodynamic parameters of Al−Li−Mg−Ti−M LW-HEAs

exhibit low densities and meet the lightweight requirements.

2.2 Alloy preparation and characterization

Pure Ti, Zn, Zr, and V metal powders with a purity ≥99.5%, as well as Al−Li (Al/Li molar ratio of 2∶1) and Mg−Li (Mg/Li molar ratio of 1∶1) master alloys, were selected as raw materials. Alloy powders with nominal compositions of $Al_{20}Li_{20}Mg_{10}Ti_{40}Zn_{10}$, $Al_{20}Li_{20}Mg_{10}Ti_{30}Zr_{20}$, and $Al_{20}Li_{20}Mg_{10}Ti_{30}V_{20}$ were prepared in a planetary ball mill using a Retsch-PM100 model. Stainless steel balls were used as the ball milling medium, the ball-to-material mass ratio was set to be 10∶1, and the alloying of #Zn was carried out at a milling speed of 300 r/min for 30 h. Since Zr and V are high melting point elements, the alloying time of #Zr and #V alloys was set to be 50 h. Stearic acid was used as a process control agent (PCA) to prevent the alloy powders from agglomerating during ball milling. Then, the as-milled powder was pressed into a disk-shaped billet with a size of d10 mm × 3 mm by a CMT5105 model universal testing machine, and the pressure was kept constant at 1 GPa for 2 min during pressing. Finally, the pressed billets were sintered without pressure using an SG-GL1200 tube furnace under the protection of an argon atmosphere. According to the theoretical melting point of the alloy, 650 and 750 °C were selected as the sintering temperature, respectively. During sintering, the billets were first heated to 100 °C at a heating rate of 5 °C/min for 1 h, then heated to the required sintering temperature for 2 h, and finally cooled to room temperature in the furnace.

The phase analysis of the alloys was carried out by the X-ray diffractometer (XRD, RigakuD/MAX−2500PC) with a Cu target. The scanning electron microscope (SEM, TESCAN VEGA3 LMH) with an energy dispersive spectroscopy (EDS) was adopted for the microstructural characterization and micro-composition analysis of the as-sintered alloys. In addition, an HV−1000 Vickers microhardness tester was used to test the room temperature microhardness of the as-sintered alloy, the applied load was 3 N, and the holding time was 15 s. In the test, ten different points were randomly selected and measured for each sample, the maximum and minimum measurement values were then removed, and the average value of the remaining test results was taken as the micro-hardness value of the alloy.

3 Results

3.1 Microstructure of as-milled Al−Li−Mg−Ti−M (M=Zn, Zr, V) LW-HEAs

Figure 2 shows the XRD patterns of the as-milled Al−Li−Mg−Ti−M (M=Zn, Zr, V) LW-HEAs. According to the XRD pattern, the #Zn alloy forms an HCP-type solid solution phase and an unknown minor phase that XRD cannot determine. The #Zr alloy forms a dual-HCP (HCP1 and HCP2) type solid solution phase. In contrast, the #V alloy only forms a single BCC-type solid solution. The experimental results confirm that the as-milled Al−Li−Mg−Ti−M (M=Zn, Zr, V) alloy powders all form a simple-phase structure. At the same time, obvious broadening of the diffraction peaks of the as-milled #Zr and #V powder samples is observed, which is deemed to be the results of grain refining due to the longer mechanical alloying time of the #Zr and #V samples than that of the #Zn sample.

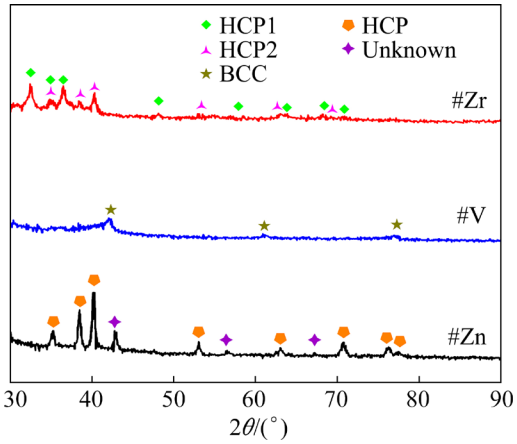

Fig. 2 XRD patterns of as-milled Al−Li−Mg−Ti−M (M=Zn, Zr, V) LW-HEAs

Moreover, it can be found that the diffraction peak position of the HCP solid solution phase in the #Zn alloy is closer to the peak position of α-Ti, suggesting that the solid solution phase has a Ti-type HCP structure. The peak positions of the HCP1 and HCP2 solid solution phases in the #Zr alloy are close to the peak positions of α-Zr and α-Ti, respectively, indicating that the dual phases have Zr-type HCP and Ti-type HCP structures, respectively. Similarly, the diffraction peak position

of the BCC phase in the #V alloy is close to the peak position of α-V, indicating that the phase has a V-type BCC structure. The solid solution phase in $AlLiMg_{0.5}Ti_{1.5}$ HEA has been reported to have a Ti-type HCP structure [4]. Therefore, it is reasonable to deduce that adding low T_m element M (Zn) to the AlLiMgTi-based alloy cannot change the solid solution phase structure in the alloy, i.e., the solid solution phase in the Al−Li−Mg−Ti−M alloy still maintains the Ti-type HCP structure of the solid solution phase in the AlLiMgTi-based alloy. In contrast, adding Zr and V elements with high T_m (higher than T_m of Ti) will change the solid solution phase structure, which tends to be the crystal structure of the high T_m elements. In other words, the elements with high T_m act as solvents in the alloy.

3.2 Microstructure of as-sintered Al−Li−Mg−Ti−M (M=Zn, Zr, V) LW-HEAs

Figure 3 shows the XRD patterns of as-sintered Al−Li−Mg−Ti−M (M=Zn, Zr, V) LW-HEAs bulk samples. Compared with the as-milled Al−Li−Mg−Ti−M (M=Zn, Zr, V) LW-HEAs, the as-sintered alloys undergo obvious phase transformation, forming new solid solutions or/and intermetallics. As shown in Fig. 3(a), the #Zn LW-HEAs form a Ti-rich HCP solid solution, τ-$Mg_{32}(Al,Zn)_{49}$, and an unknown phase after sintering at 650 °C. When the sintering temperature increases to 750 °C, the Ti-rich HCP solid solution and τ-$Mg_{32}(Al,Zn)_{49}$ phase disappear, γ-$Al_{12}Mg_{17}$ phase, a small amount of β-$AlTi_3$ intermetallic and an unknown phase are formed. Figure 3(b) shows the XRD patterns of the sintered #Zr LW-HEAs. It can be found that the #Zr LW-HEAs sintered at 650 and 750 °C both retain the dual-HCP solid solution (HCP1 and HCP2) structure of the as-milled LW-HEA and only one unknown phase precipitates, which means that the alloy has high phase stability. From the XRD patterns of the as-sintered #V LW-HEAs in Fig. 3(c), it can be found that when the sintering temperature is 650 °C, the #V alloy consists of Ti-rich HCP solid solution, V-rich BCC solid solution, and a small amount of β-$AlTi_3$ and γ-$Al_{12}Mg_{17}$ intermetallics. When the sintering temperature increases to 750 °C, HCP phase disappears, and #V alloy is mainly composed of β-$AlTi_3$, a small amount of γ-$Al_{12}Mg_{17}$ intermetallic, and BCC solid solution.

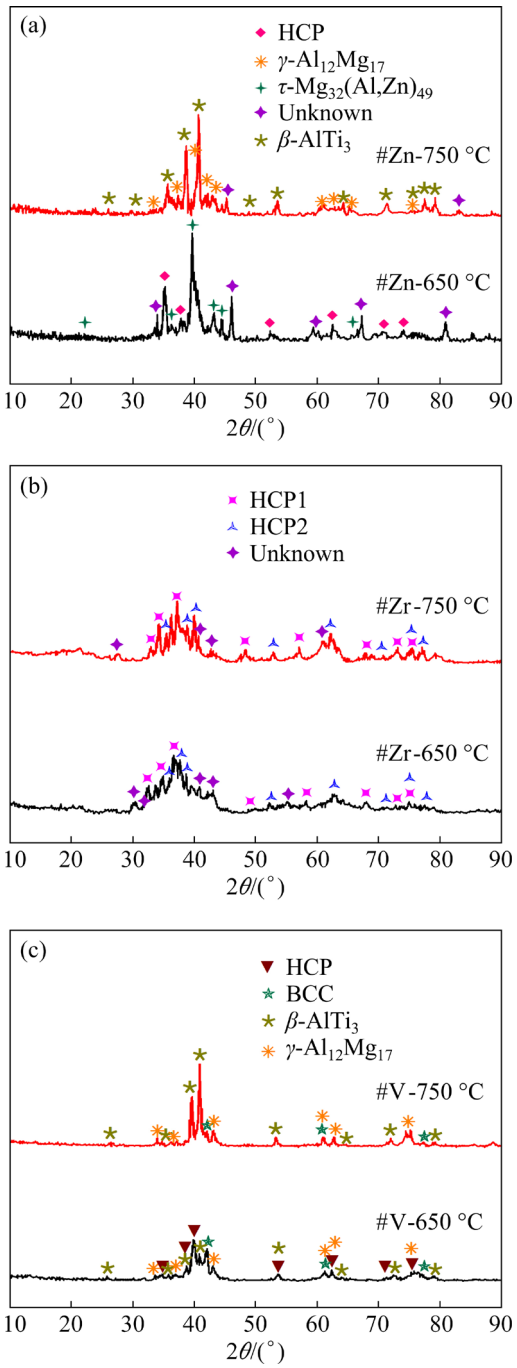

Fig. 3 XRD patterns of as-sintered Al−Li−Mg−Ti−M (M=Zn, Zr, V) LW-HEAs: (a) #Zn; (b) #Zr; (c) #V

The SEM backscattered electron images and EDS analysis results of the as-sintered Al−Li−Mg−Ti−M (M=Zn, Zr, V) LW-HEAs are shown in Fig. 4 and Table 3, respectively. It can be seen from the figure that the microstructures of #Zn and #Zr LW-HEAs sintered at 650 and 750 °C are relatively dense and do not show obvious pores. However, the as-sintered bulk #V LW-HEAs show less densification degree and there are more pores in the microstructure. According to the EDS mappings in

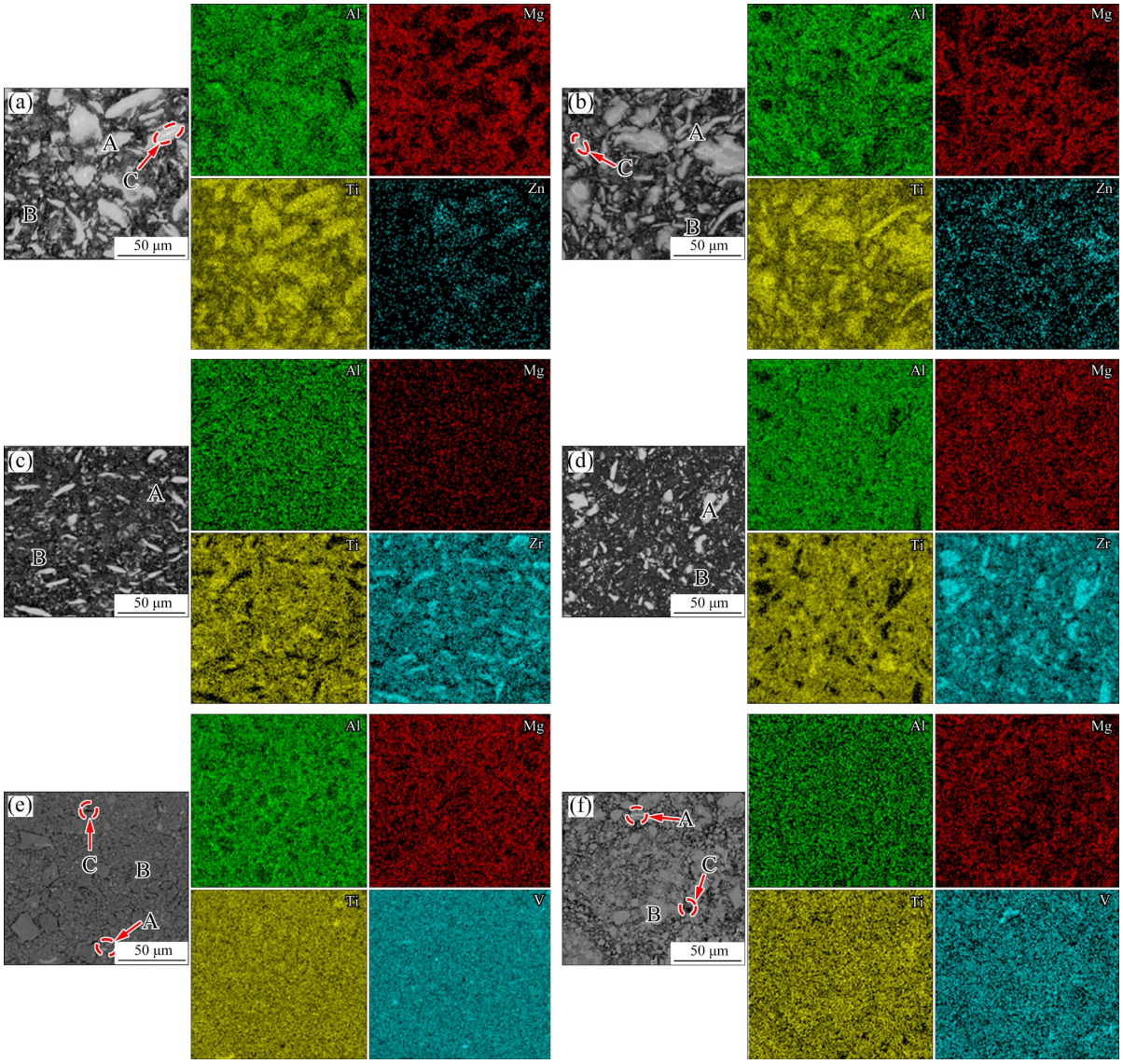

Fig. 4 SEM images and EDS mappings of as-sintered Al−Li−Mg−Ti−M (M=Zn, Zr, V) LW-HEAs: (a) #Zn-750 °C; (b) #Zn-650 °C; (c) #Zr-750 °C; (d) #Zr-650 °C; (e) #V-750 °C; (f) #V-650 °C

Fig. 4, both the as-sintered #Zn and #Zr alloys show an evident element segregation phenomenon, while the element distribution in the #V alloy is relatively uniform. It can be figured out from Fig. 4(a) and Table 3 that the #Zn-750 °C alloy has at least three regions with different compositional contrasts (marked as A, B, and C, respectively). Ti element is segregated in regions A and C, and Mg element is segregated in region B. Combining with the XRD pattern in Fig. 3(a), it can be determined that the off-white region A is β-$AlTi_3$ phase, while the gray black region B is γ-$Al_{12}Mg_{17}$ phase. The bright white region C is a Ti-rich HCP-type solid solution phase, but the volume fraction of the HCP phase is too small to be identified by XRD. As shown in Fig. 4(b), there are also at least three regions with different composition contrasts in the #Zn-650 °C alloy (marked as A, B, and C, respectively). The off-white region A is the HCP phase. And the gray-black region B is the τ-$Mg_{32}(Al,Zn)_{49}$ phase rich in Mg, Al, and Zn. In addition, the EDS analysis results in Table 3 show that the bright white region C is rich in Zn, Ti, and Al elements, corresponding to the unknown phase calibrated in Fig. 3(a). The formation of τ-$Mg_{32}(Al,Zn)_{49}$ intermetallic is because Mg and Al, Zn elements have strong tendency to form complex intermetallic phases. In addition, the binary mixing enthalpy between Al and Ti elements is more negative (Table 2), so Al−Ti-based β phase is easy to form

Table 3 EDS analysis results of as-sintered Al−Li−Mg−Ti−M (M=Zn, Zr, V) LW-HEAs in Fig. 4

Alloy	Region	Composition/at.%						Phase
		Al	Mg	Ti	Zn	Zr	V	
#Zn-750 °C	A	21.91	0	73.96	4.12	−	−	β-$AlTi_3$
	B	37.78	56.21	6.01	0	−	−	γ-$Al_{12}Mg_{17}$
	C	6.09	0	83.31	10.61	−	−	HCP
#Zn-650 °C	A	16.28	4.91	58.77	20.04	−	−	HCP
	B	47.83	32.70	12.6	6.87	−	−	τ-$Mg_{32}(Al,Zn)_{49}$
	C	15.61	3.16	36.10	45.13	−	−	Unknown phase
#Zr-750 °C	A	30.90	3.23	10.38	−	55.49	−	HCP1
	B	27.55	5.84	59.58	−	7.03	−	HCP2
#Zr-650 °C	A	31.76	2.87	11.52	−	53.85	−	HCP1
	B	28.21	3.19	65.36	−	3.24	−	HCP2
#V-750 °C	A	5.45	6.74	6.84	−	−	80.97	BCC
	B	27.27	8.38	40.96	−	−	23.39	β-$AlTi_3$
	C	32.50	54.59	7.42	−	−	5.49	γ-$Al_{12}Mg_{17}$
#V-650 °C	A	7.88	7.13	3.64	−	−	81.35	BCC
	B	25.77	9.13	40.95	−	−	24.16	HCP
	C	34.64	53.73	6.34	−	−	5.29	γ-$Al_{12}Mg_{17}$

and relatively thermodynamically stable. Moreover, according to Table 3, the HCP phase in the #Zn-650 °C alloy contains a certain amount of Mg element, while no Mg element is detected in the HCP phase in the #Zn-750 °C alloy. In other words, the increase of temperature promotes the diffusive precipitation of Mg from the HCP phase and the formation of intermetallic with other elements.

Figures 4(c) and (d) show the EDS mappings of the #Zr-750 °C and #Zr-650 °C alloys, respectively. It can be found that both the #Zr alloys sintered at 650 and 750 °C exhibit two regions (marked as A and B) with different compositional contrasts. Combining the XRD patterns of Fig. 3(b) and the EDS analysis results in Table 3, it can be determined that the bright region A is the Zr-rich HCP solid solution phase, and the dark region B is the Ti-rich HCP solid solution phase. No phase transition occurs after sintering, indicating that the #Zr alloy with dual-HCP solid solution phase has better high-temperature phase stability.

Figures 4(e) and (f) show the EDS mappings of the #V-750 °C and #V-650 °C alloys, respectively. It can be seen that there are at least three regions (marked as A, B, and C, respectively) with different compositional contrasts in both the #V-750 °C and V-650 °C alloys. Combined with the XRD pattern of Fig. 3(c) and the EDS analysis results in Table 3, it can be determined that the bright white region A, the off-white region B, and the dark black region C in the #V-750 °C alloy are V-rich BCC phase, β-$AlTi_3$ phase, and γ-$Al_{12}Mg_{17}$ phase, respectively. In the #Zn and #V alloys, the Ti-rich HCP phase transforms into β-$AlTi_3$ and γ-$Al_{12}Mg_{17}$ phases after sintering at 750 °C, while in the #Zr alloy the phase transformation does not occur. Therefore, the Ti-rich HCP phases in the #Zn and #V alloys are less stable than those in the #Zr alloys. In addition, it can be determined that regions A, B, and C in the #V-650 °C alloy are the V-rich BCC phase, Ti-rich HCP phase, and γ-$Al_{12}Mg_{17}$ phase, respectively. It is worth noting that the β-$AlTi_3$ phase in the #V-650 °C alloy detected in XRD cannot be identified in the SEM microstructure, possibly because the phase volume fraction in the detection area is too small or the composition contrast between the β-$AlTi_3$ and Ti-rich HCP phases is not noticeable.

Except for the #Zr alloys, the phase compositions of LW-HEAs are closely related to the sintering temperature, and the microstructures of alloys sintered at different temperatures are

significantly different. The higher the phase stability, the smaller the difference in the microstructures sintered at different temperatures. The thermal stability of low-order (binary and ternary subsystems) phases is crucial to the phase stability of HEA systems [22], i.e., intermetallics with a strong tendency to form in binary and ternary systems are also more prone to precipitate in multicomponent alloy systems. γ-$Al_{12}Mg_{17}$ and τ-$Mg_{32}(Al,Zn)_{49}$ phases prefer to form in Mg−Al binary and Mg−Al−Zn ternary alloy systems [23,24], such that they also tend to precipitate in Al−Li−Mg−Ti-M (M=Zn, Zr, V) LW-HEAs.

3.3 Mechanical properties of Al−Li−Mg−Ti−M (M=Zn, Zr, V) LW-HEAs

Figure 5(a) shows the microhardness (HV) of as-sintered Al−Li−Mg−Ti−M (M=Zn, V, Zr) LW-HEAs. It can be seen that the microhardness of Al−Li−Mg−Ti−M (M=Zn, V, Zr) LW-HEAs increases with the increase of sintering temperature. Moreover, under the same sintering temperature, the microhardness of the #V alloy is the highest, followed by the microhardness of the #Zr alloy, and the microhardness of the #Zn alloy is the lowest. To explore the mechanical properties of Al−Li−Mg−Ti−M (M=Zn, V, Zr) LW-HEAs, the yield strength (σ_y) is calculated by the empirical formula [25]:

$$HV=3\sigma_y \quad (9)$$

Figure 5(b) shows the yield strength of as-sintered Al−Li−Mg−Ti−M (M=Zn, V, Zr) LW-HEAs, and Fig. 6 shows the specific yield strength (ratio of yield strength/density) of as-sintered Al−Li−Mg−Ti−M (M=Zn, V, Zr) LW-HEAs. Consistent with the change in hardness, the strength and specific strength of Al−Li−Mg−Ti−M (M=Zn, V, Zr) LW-HEAs increase with the increase of sintering temperature. As for the same sintering temperature, the #V alloy has the highest strength and specific strength and the #Zn alloy has the lowest ones. The specific strength of the alloys is in the range of 161.1−625.2 MPa·cm^3/g. Figure 7 shows the specific yield strength versus the density of some LW-HEAs [10,14,15,26−31], AZ31 [32], Inconel [15], and Ti−6Al−4V [15] alloys. The as-sintered Al−Li−Mg−Ti−M (M=Zn, V, Zr) alloy has a lower density and higher specific strength, and the specific strength of the alloy is higher than most of the reported LW-HEAs, magnesium alloys, titanium alloys, and nickel-based alloys. Except for the #Zn-650 °C and #Zr-650 °C alloys, the specific strengths of the other alloys prepared in this work are higher than that of Ti−6Al−4V alloy. Among them, the #V-750 °C alloy has the highest specific strength (up to 625.2 MPa·cm^3/g), 2.5 times that of Ti−6Al−4V alloy and just lower than that of $Al_{20}Be_{20}Fe_{10}Si_{15}Ti_{35}$ and $Al_{20}Li_{20}Mg_{10}Ti_{30}Sc_{20}$ LW-HEAs.

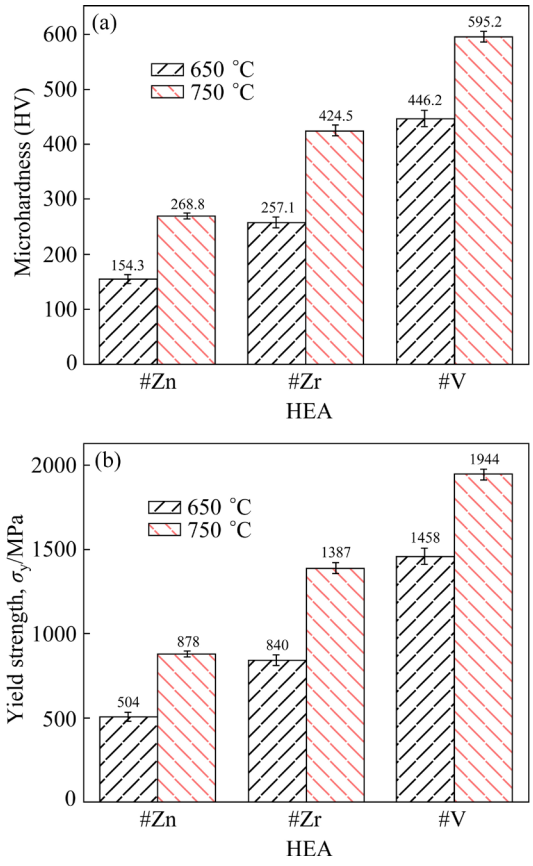

Fig. 5 Microhardness (a) and yield strength (b) of as-sintered Al−Li−Mg−Ti−M (M=Zn, Zr, V) LW-HEAs

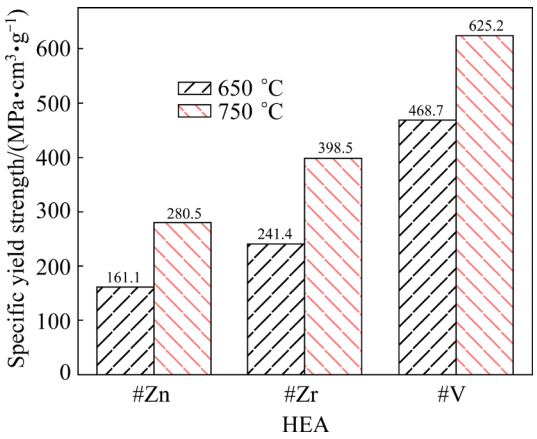

Fig. 6 Specific yield strength of as-sintered Al−Li−Mg−Ti−M (M=Zn, Zr, V) LW-HEAs

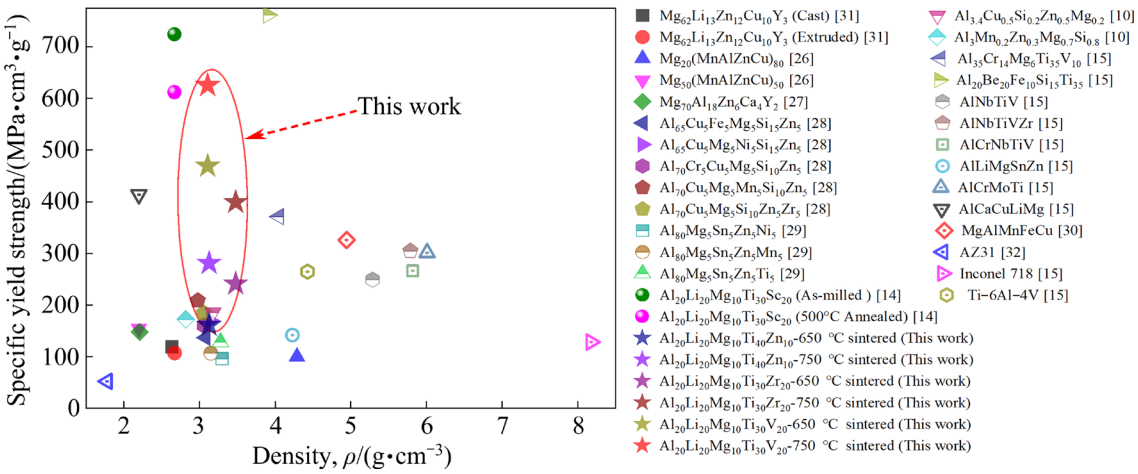

Fig. 7 Specific yield strength versus density of some LW-HEAs [10,14,15,26−31], AZ31 [32], Inconel [15], and Ti−6Al−4V [15] alloys

4 Discussion

4.1 Elemental dissolution−phase structure correlation

Understanding and discussing the elemental dissolution law can help predict the phase structure of the as-milled HEAs. The inherent physicochemical properties of the component elements [12,33,34], such as melting point (T_m), atomic radius (r), self-diffusion coefficient, ductility [12,33−35], especially T_m [33−35], play an important role in the elemental dissolution, alloying, and phase formation during the mechanical alloying. Usually, the diffusion rate of elements with high T_m is lower than that with low T_m due to the stronger interatomic binding energy [33,34,36]. As a consequence, the elements with high T_m tend to serve as solvents due to their slow diffusion rate. Elements with low T_m will gradually diffuse into and replace the lattice positions of elements with high T_m during ball milling process [33,34]. Among the component elements of the #Zn and #V alloys, Ti and V have the highest T_m, respectively, and consequently act as solvents, causing the peaks of the final solid solution to approach the HCP Ti ($2\theta_{(101)peak}$=40.16°) and BCC V ($2\theta_{(110)\ peak}$=42.20°) peaks (Fig. 2), respectively. Similar to the #Zn and #V alloys, the dependence of the as-milled solid solution structure on the crystal structure of the highest T_m component has also been reported for many Mg-containing HEAs [12,37−39]. However, although Zr has the highest T_m in the #Zr alloys, a dual-phase solid solution structure, Zr-type HCP and Ti-type HCP, is obtained after ball milling. This is largely attributed to the fact that Zr and Ti have a similar magnitude order of self-diffusion coefficients [40], and thus they can both act as solvents. Therefore, the solid solution phase structure of the as-milled alloys depends not only on the crystal structure of the highest T_m element but also the elemental self-diffusion coefficients.

4.2 Phase stability

Based on the XRD and SEM results, it can be found that the as-milled alloys precipitate intermetallics after sintering, which implies that the solid solutions obtained from ball milling are metastable. Table 4 lists the phase statistics of the as-milled and as-sintered Al−Li−Mg−Ti−M (M=Zn, Zr, V) LW-HEAs to visualize the phase evolution of the alloy and analyze the stability of the solid solution phases. According to Table 4, only τ-$Mg_{32}(Al,Zn)_{49}$ precipitates from the #Zn alloys after sintering at 650 °C, whereas γ-$Al_{12}Mg_{17}$ and β-$AlTi_3$ phases precipitate after sintering at 750 °C. The #V alloy forms the Ti-type HCP phase, γ-$Al_{12}Mg_{17}$, and β-$AlTi_3$ phases after sintering at 650 °C, which is a complex phase transition. Therefore, the alloy has the lowest solid solution phase stability. However, only one unknown phase precipitates in the #Zr alloy after sintering at 650 and 750 °C, and the major structure remains a dual-phase solid solution, implying a high phase stability. It should be mentioned that the as-milled $Al_{20}Li_{20}Mg_{10}Ti_{30}Sc_{20}$ LW-HEA with a single HCP

phase precipitates more intermetallics after sintering at 650 °C, including γ-$Mg_{17}Al_{12}$, β-$AlTi_3$, and AlTi phases [4]. Therefore, the #Zr alloys exhibit higher phase stability than $Al_{20}Li_{20}Mg_{10}Ti_{30}Sc_{20}$ alloy.

From the above results, it can be seen that the #Zr alloy has the highest thermal stability, while #V has the worst thermal stability. It is believed that that the T_m of HEAs plays an important role in the phase stability. Normally, HEAs with high T_m exhibit excellent thermal stability. Among the three alloys in this study, the low T_m of Zn element leads to a low T_m of 1215.4 K for the #Zn alloy. However, although the difference in the T_m between the #Zr and #V alloys is slight (Fig. 8), the difference in thermal stability is significant.

In multicomponent solid solutions, high lattice distortions can exacerbate solid solution decomposition, reducing the solid solution phase stability [41,42]. Both atomic size difference δ and parameter α_2 proposed in Refs. [41,42] can describe the lattice distortion:

$$\alpha_2=\sum_{j\geq i}^{n}\frac{c_i c_j\left|r_i+r_j-2\bar{r}\right|}{2\bar{r}} \tag{10}$$

where $\bar{r}$ is the average atomic radius.

Figure 8 compares the δ and α_2 values of Al−Li−Mg−Ti−M (M=Zn, Zr, V) LW-HEAs. The #V alloys have the largest lattice distortion, which means that phase decomposition degree is the intensest and phase stability is the lowest. Compared to the #V alloy, the #Zn alloy has lower lattice distortion and thus higher phase stability. It should be mentioned that in the calculation of the δ and α_2 values for the #Zr alloy which has a dual HCP solid solution structure, the elemental content of the whole alloy is taken rather than the elemental content of the respective components in the Ti- and Zr-type HCP solid solutions, which brings about a certain error, and might affect the accuracy of the evaluation. In fact, due to the formation of a dual-phase solid solution structure in the #Zr alloys, the solute content should be lower than that of a single-phase solid solution structure, and the lattice

Table 4 Phase statistics of as-milled and as-sintered Al−Li−Mg−Ti−M (M=Zn, Zr, V) LW-HEAs ("√" represents presence and "×" represents absence)

Alloy	Ti-type HCP	Zr-type HCP	V-type BCC	τ-$Mg_{32}(Al,Zn)_{49}$	Unknown phase	γ-$Al_{12}Mg_{17}$	β-$AlTi_3$
#Zn-milled	√			×	√	×	×
#Zn-650 °C	√			√	√	×	×
#Zn-750 °C	√			×	√	√	√
#Zr-milled	√	√			×	×	×
#Zr-650 °C	√	√			√	×	×
#Zr-750 °C	√	√			√	×	×
#V-milled	×		√		×	×	×
#V-650 °C	√		√		×	√	√
#V-750 °C	×		√		×	√	√

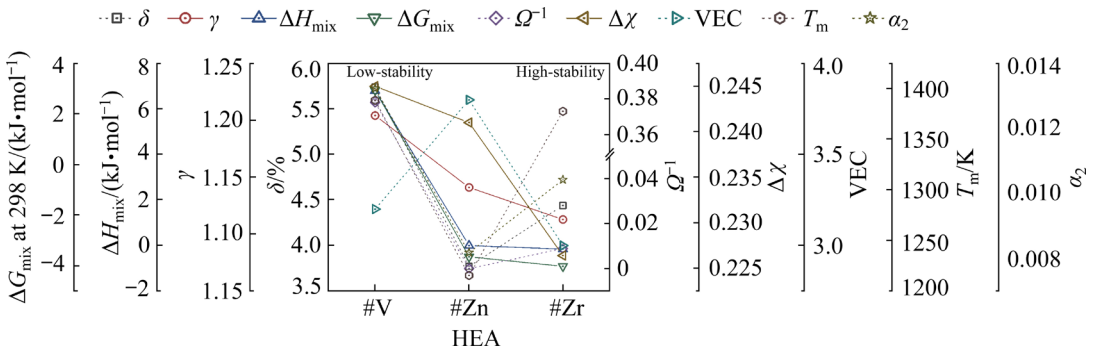

Fig. 8 Comparison of calculated empirical parameters for #V, #Zn, and #Zr alloys (γ is the stacking parameter; α_2 is the lattice distortion parameter)

distortion of a dual-phase HCP structure should be lower than the calculated value. If half of the content of each element Al, Li, and Mg goes into the Ti- and Zr-type solid solutions, the stoichiometric formulas of the Ti- and Zr-type solid solutions will be $Al_{10}Li_{10}Mg_5Ti_{30}$ and $Al_{10}Li_{10}Mg_5Zr_{20}$, respectively, whose lattice distortion parameter α_2 can be calculated as 0.006091 and 0.007538, respectively. Compared to a complete single-phase solid solution, whose lattice distortion parameter α_2 is calculated to be 0.010421, the value of the dual-phase alloy is apparently lower. Besides, a dual-phase structure effectively decreases the lattice distortion caused by the atomic size differences of the constituent elements [43].

It should be noted that δ represents the average effect of the atomic size difference of all elements in the alloy. However, in multicomponent alloys, the phase stability may be mainly determined by the atoms with the largest (r_L) and smallest (r_S) sizes. WANG et al [44] constructed a stacking parameter (γ) using r_L and r_S to characterize the atomic stacking effect in multicomponent alloys:

$$\gamma=1-\sqrt{\frac{(r_S+\bar{r})^2-\bar{r}^2}{(r_S+r)^2}}\Bigg/\left[1-\sqrt{\frac{(r_L+\bar{r})^2-\bar{r}^2}{(r_L+r)^2}}\right] \tag{11}$$

As shown in Fig. 8, the γ parameter is closely related to the phase stability of Al−Li−Mg−Ti−M (M=Zn, Zr, V) LW-HEAs. The smaller the value of γ, the higher the phase stability of the solid solution. The γ values of #V, #Zn, and #Zr alloys are 1.204, 1.141, and 1.113, respectively. The atomic size of the fifth element M affects the phase stability by influencing the atomic stacking effect of the alloy. To visualize the effect of the atomic size of element M, Fig. 9 shows the atomic sizes of the elements in Al−Li−Mg−Ti−M LW-HEAs. Here, a window is created with the range of atomic radii for the base elements Al, Li, Mg, and Ti. Connecting the phase stability for Al−Li−Mg−Ti−M LW-HEAs, it is easy to see that the closer the atomic radius of the element M to the window, the higher the phase stability. That is, the element M with an atomic radius close to the window is the element that enhances the phase stability of Al−Li−Mg−Ti−M LW-HEAs most obviously, such as Zr.

Generally, the larger the Ω value, the more pronounced the high entropy effect, so the higher the solid solution phase stability [45]. The #V alloys have the lowest Ω values (even below the critical value of 10 proposed by YANG et al [46]), implying the worst phase stability. However, there is a difference in the actual results when evaluating the #Zn and #Zr alloy's phase stability by Ω values, i.e., the #Zr alloy has a lower Ω, but its phase stability is higher. VEC has also been widely used to evaluate the phase stability of most HEAs [47], such as 3d transition metal HEAs and refractory HEAs, and the criterion is directly related to the phase type. In this work, due to different types and amounts of solid solution phases formed in the as-milled Al−Li−Mg−Ti−M (M=Zn, Zr, V) LW-HEAs, it is not possible to directly establish a correlation between the phase stability of Al−Li−Mg−Ti−M (M=Zn, Zr, V) LW-HEAs and the VEC value. According to Fig. 8, there is a better correlation between the phase stability of Al−Li−Mg−Ti−M (M=Zn, Zr, V) LW-HEAs and the $\Delta\chi$ value. The smaller the $\Delta\chi$ value, the more favorable the formation of a multicomponent solid solution and the higher the phase stability.

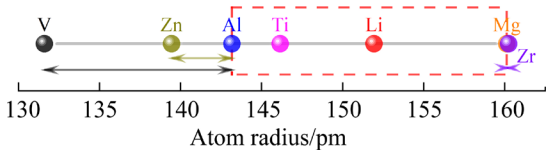

Fig. 9 Atomic sizes of elements in Al−Li−Mg−Ti−M LW-HEAs

To illustrate the stability of LW-HEAs, Gibbs free energy change (ΔG_{mix}) is analyzed. As we know, ΔG_{mix} for multicomponent alloy system can be expressed as [48]

$$\Delta G_{mix}=\Delta H_{mix}-T\Delta S_{mix} \tag{12}$$

where T is the thermodynamic temperature. According to Fig. 8, ΔH_{mix} and ΔG_{mix} values are closely related to the phase stability of Al−Li−Mg−Ti−M (M=Zn, Zr, V) LW-HEAs. ΔH_{mix} represents the average atomic interaction of HEA. A positive ΔH_{mix} implies a weakening interatomic interaction, resulting a decreased thermal stability of the alloy. The #Zr alloy has the lowest and negative ΔH_{mix}, which means that it has stronger atomic interactions, and thus a higher thermal stability. In addition, based on the ΔG_{mix} results, the #Zr alloy has the lowest system energy, implying the highest stability.

In conclusion, atomic stacking effects, electronegativity differences, mixing enthalpy, and Gibbs

free energy change play an important role in evaluating the phase stability of the current Al−Li−Mg−Ti−M (M=Zn, Zr, V) LW-HEAs, i.e., element M affects the phase stability of the alloys via atomic stacking effects, electronegativity differences, mixing enthalpy, and Gibbs free energy change.

4.3 Enhanced mechanical properties

To analyze the properties of the LW-HEAs, the microhardness of the phases present in the LW-HEAs is calculated using the model proposed by CHEN et al [49]:

$$HV=2(k^2G)^{0.585}-3 \quad (13)$$

$$k=G/B \quad (14)$$

where B is the bulk modulus and G is the shear modulus. Table 5 lists the values of B, G, B/G, and microhardness for the phases present in Al−Li−Mg−Ti−M (M=Zn, Zr, V) LW-HEAs. It should be noted that here in the calculation, the parameters of α-Ti, α-Zr, and α-V are taken as those of the Ti-rich HCP phase, Zr-rich HCP phase, and V-rich BCC phase in the alloys, respectively. Since these phases actually have multiple solute elements, the solid solution strengthening effect will cause a higher HV than the calculated values of these phases.

According to Table 5, the β-$AlTi_3$ has the highest hardness (8.01 GPa). The hardness of the Ti-rich HCP, γ-$Al_{12}Mg_{17}$, V-rich BCC, and Zr-rich HCP phases is 6.99, 6.08, 4.08, and 2.06 GPa, respectively. But the hardness of τ-$Mg_{32}(Al,Zn)_{49}$ phase is very low, only 1.17−4.06 GPa, which means that τ-$Mg_{32}(Al,Zn)_{49}$ phase will deteriorate the hardness and strength of the alloy. According to the mixing rules, the higher the hard-phase content in the alloy is, the higher the hardness and strength are.

Although there are Ti-rich HCP phases with high hardness in the #Zn-650 °C alloy, the bonding between powder particles is weak due to the low sintering temperature, resulting in the lowest hardness; while in the #Zn-750 °C alloy, β-$AlTi_3$ phase precipitates, which enhances the hardness and strength of the alloy. Both #Zr-650 °C and #Zr-750 °C alloys retain the dual-HCP structure (Ti-rich HCP phase and Zr-rich HCP phase) and only a trace amount of unknown phase precipitates. Therefore, the solid solution strengthening of the HCP phase and the precipitation strengthening of the unknown phase are the main strengthening means of the #Zr alloys. The #V-650 °C alloy contains high hardness β-$AlTi_3$, HCP, and BCC phases, so the alloy has higher hardness and strength than the #Zn and #Zr alloys. As the sintering temperature increases, the particles in the #V-750 °C alloy have better bonding than those in the #V-650 °C alloy, and β-$AlTi_3$ phase precipitates, thus increasing the hardness and strength. Therefore, the solid solution strengthening of the BCC phase and the precipitation strengthening of the β-$AlTi_3$ phase are the main strengthening means of the alloy.

Plasticity is also an important mechanical property parameter of materials. According to the mixing law, the alloys with more ductile phases have a better plasticity than those with more brittle phases. The ratio of bulk modulus to shear modulus B/G and Poisson's ratio (ν) can be used to determine the ductile and brittle characters of a phase [56]. According to the B/G–ν criterion: the phases with $B/G > 1.75$ and $\nu > 0.26$ can be regarded as ductile characteristics, while the phases with $B/G < 1.75$ and $\nu < 0.26$ can be regarded as brittle characteristics. Figure 10 shows the B/G–ν relationship of the phases in the Al−Li−Mg−Ti−M (M=Zn, Zr, V) LW-HEAs. According to the B/G–ν criterion, phases, except for the γ-$Al_{12}Mg_{17}$ phase, have ductile characteristics. According to the phase

Table 5 Values of B, G, B/G, ν, and HV for phases present in Al−Li−Mg−Ti−M (M=Zn, Zr, V) LW-HEAs

Phase	B/GPa	G/GPa	B/G	ν	HV/GPa
β-$AlTi_3$ [50]	112.83	61.72	1.83	0.269	8.01
γ-$Mg_{17}Al_{12}$ [51]	51.30	32.7	1.57	0.240	6.08
Ti-type HCP (α-Ti) [52]	106.00	56.00	1.89	0.270	6.99
Zr-type HCP (α-Zr) [53]	86.33	33.14	2.60	0.330	2.06
V-type BCC (α-V) [54]	164.60	61.70	2.70	0.330	4.08
τ-$Mg_{32}(Al,Zn)_{49}$ [55]	73.71−80.69	28.97−37.96	2.10−2.77	0.290−0.330	1.17−4.06

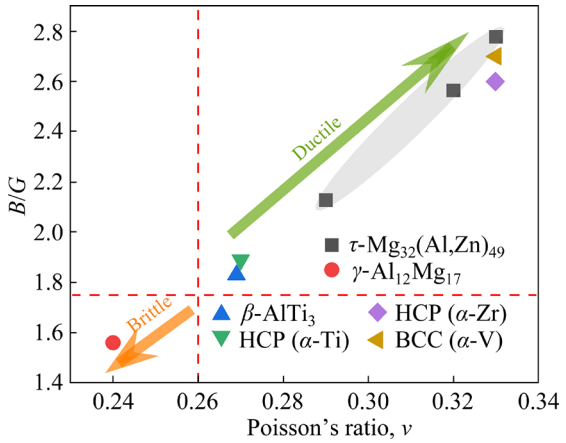

Fig. 10 B/G versus ν for phases present in Al−Li−Mg−Ti−M (M=Zn, Zr, V) LW-HEAs

statistics of the sintered Al−Li−Mg−Ti−M (M=Zn, Zr, V) LW-HEAs, the absence of the brittle γ-$Al_{12}Mg_{17}$ phases in the #Zr alloys sintered at 650 and 750 °C, and in the #Zn alloys sintered at 650 °C, implies that the #Zr-650 °C, #Zr-750 °C, and #Zn-650 °C alloys have excellent plasticity potential.

5 Conclusions

(1) The as-milled Al−Li−Mg−Ti−M (M=Zn, Zr, V) LW-HEAs formed a relatively simple solid solution structure. The solid solution structure depends on the room-temperature crystal structure of the highest T_m element, and the elemental self-diffusion coefficient. Among them, the #Zn alloy forms a Ti-type HCP solid solution phase and an unknown phase, the #Zr alloy forms a dual-phase HCP phase structure, and the #V alloy forms a single V-type BCC solid solution phase structure.

(2) After cold-press sintering, the #Zn and #V alloys undergo obvious phase transformation; while the #Zr alloy with dual-HCP phases exhibits the best phase stability during the heat treatment, and the #Zr alloy still maintains the dual-HCP phase structure even after sintering at 750 °C.

(3) Atomic stacking effects, electronegativity differences, mixing enthalpy change, and Gibbs free energy change play an important role in evaluating the phase stability of the Al−Li−Mg−Ti−M (M=Zn, Zr, V) LW-HEAs. The #Zr alloy with a dual-HCP structure has the highest phase stability.

(4) All the sintered Al−Li−Mg−Ti−M (M=Zn, Zr, V) LW-HEAs exhibit high microhardness, strength, and specific strength. The hardness and specific strength increase with the increase of the sintering temperature. Additionally, the #V-750 °C alloy exhibits the highest microhardness and specific strength, reaching HV 595.2 and 625 MPa·cm^3/g, respectively. The #Zr-650 °C, #Zr-750 °C, and #Zn-650 °C alloys reveal excellent plasticity potential based on the B/G−ν criterion.

CRediT authorship contribution statement

Quan DONG: Investigation, Methodology, Data curation, Writing − Original draft, Review & editing; **Meng LI:** Investigation, Methodology, Data curation, Writing − Original draft; **Yu-fei ZHANG:** Data curation, Writing − Review & editing; **Jing ZHANG:** Investigation, Supervision, Methodology, Data curation, Funding acquisition, Writing − Review & editing.

Declaration of competing interest

The authors declare that they have no known competing financial interests or personal relationships that could have appeared to influence the work reported in this paper.

Data availability

Data will be available on request.

Acknowledgments

This work was financially supported by China Aeronautical Science Foundation (No. 2023Z0530Q9002), and the Program for Chongqing Talents, China (No. cstc2024ycjh-bgzxm0066).

References

[1] ZHANG Guo-jia, WANG Ming-liang, LU Yi-ping, WANG Tong-min, LI Ting-ju. Microstructural stability and mechanical properties of BCC-based $Fe_{3.5}Cr_{1.5}NiAl_{0.8}$ multicomponent alloy [J]. Transactions of Nonferrous Metals Society of China, 2023, 33: 2461−2470.

[2] MA Zi-hao, HOU Bing, QIN Dong-yang, LI Yu-long. Effect of strain rate on mechanical properties of HCP/FCC dual-phase $CoCrFeNiNb_{0.5}$ high-entropy alloy [J]. Transactions of Nonferrous Metals Society of China, 2023, 33: 1144−1155.

[3] YAN Xue, XU Jian-yan, GUAN Xiang-he, HAN Bing-yuan, ZHANG Cheng, CUI Zi-ruo, LIANG Wen-ping. Optimization of microstructure and properties of laser sintered $Ni_{30}Cr_{25}Al_{15}Co_{15}Mo_5Ti_5Y_5$ high-entropy alloy coatings via controlling plasma [J]. Transactions of Nonferrous Metals Society of China, 2023, 33: 168−188.

[4] DONG Quan, LI Meng, LIU Xue-jian, ZHANG Yu-fei,

ZHANG Jing. Microstructure, phase stability, and mechanical properties of $(AlLiMg_{0.5}Ti_{1.5})_{100-x}Sc_x$ lightweight high-entropy alloys [J]. Intermetallics, 2024, 164: 108089.

[5] CHUANG M H, TSAI M H, WANG W R, LIN S J, YEH J W. Microstructure and wear behavior of $Al_xCo_{1.5}CrFeNi_{1.5}Tiy$ high-entropy alloys [J]. Acta Materialia, 2011, 59: 6308−6317.

[6] YE Y X, LIU C Z, WANG H, NIEH T G. Friction and wear behavior of a single-phase equiatomic TiZrHfNb high-entropy alloy studied using a nanoscratch technique [J]. Acta Materialia, 2018, 147: 78−89.

[7] LI Meng-jiao, CHEN Qing-jun, CUI Xia, PENG Xin-yuan, HUANG Guo-sheng. Evaluation of corrosion resistance of the single-phase light refractory high entropy alloy $TiCrVNb_{0.5}Al_{0.5}$ in chloride environment [J]. Journal of Alloys and Compounds, 2021, 857: 158278.

[8] FU Yu, LI Jun, LUO Hong, DU Cui-wei, LI Xiao-gang. Recent advances on environmental corrosion behavior and mechanism of high-entropy alloys [J]. Journal of Materials Science & Technology, 2021, 80: 217−233.

[9] HUANG Rui, WANG Wei, LI Tian-xin, ZHANG Ling-kun, AMAR A, CHEN Xiao-hu, REN Zheng, LU Yi-ping. A novel AlMoNbHfTi refractory high-entropy alloy with superior ductility [J]. Journal of Alloys and Compounds, 2023, 940: 168821.

[10] MITRICĂ D, BADEA I C, OLARU M T, CARLAN B A, VONICA D, BURADA M, GEANTA V, ROTARIU A N, STOICIU F, BADILITA V, LICU L. Modeling and experimental results of selected lightweight complex concentrated alloys, before and after heat treatment [J]. Materials, 2020, 13: 4330.

[11] JI Cheng-wei, MA Ai-bin, JIANG Jing-hua. Mechanical properties and corrosion behavior of novel Al−Mg−Zn−Cu−Si lightweight high entropy alloys [J]. Journal of Alloys and Compounds, 2022, 900: 163508.

[12] SINGH N, SHADANGI Y, SHIVAM V, MUKHOPADHYAY N K. MgAlSiCrFeNi low-density high entropy alloy processed by mechanical alloying and spark plasma sintering: Effect on phase evolution and thermal stability [J]. Journal of Alloys and Compounds, 2021, 875: 159923.

[13] JIA Y, JIA Y, WU S, MA X, WANG G. Novel ultralight-weight complex concentrated alloys with high strength [J]. Materials, 2019, 12: 1136.

[14] YOUSSEF K M, ZADDACH A J, NIU C N, IRVING D L, KOCH C C. A novel low-density, high-hardness, high-entropy alloy with close-packed single-phase nanocrystalline structures [J]. Materials Research Letters, 2014, 3: 95−99.

[15] CHAUHAN P, YEBAJI S, NADAKUDURU V N, SHANMUGASUNDARAM T. Development of a novel light weight Al35Cr14Mg6Ti35V10 high entropy alloy using mechanical alloying and spark plasma sintering [J]. Journal of Alloys and Compounds, 2020, 820: 153367.

[16] MIRACLE D B, SENKOV O N. A critical review of high entropy alloys and related concepts [J]. Acta Materialia, 2017, 122: 448−511.

[17] HEYDARI H, TAJALLY M, HABIBOLAHZADEH A. Computational analysis of novel AlLiMgTiX light high entropy alloys [J]. Materials Chemistry and Physics, 2022, 280: 125834.

[18] TIAN Yu-sheng, ZHOU Wen-zhe, TAN Qing-biao, WU Ming-xu, QIAO Shen, ZHU Guo-liang, DONG An-ping, SHU Da, SUN Bao-de. A review of refractory high-entropy alloys [J]. Transactions of Nonferrous Metals Society of China, 2022, 32: 3487−3515.

[19] TAKEUCHI A, INOUE A. Classification of bulk metallic glasses by atomic size difference, heat of mixing and period of constituent elements and its application to characterization of the main alloying element [J]. Materials Transactions, 2005, 46: 2817−2829.

[20] LI Ze-zhou, ZHAO Shi-teng, RITCHIE R O, MEYERS M A. Mechanical properties of high-entropy alloys with emphasis on face-centered cubic alloys [J]. Progress in Materials Science, 2019, 102: 296−345.

[21] SENKOV O N, WILKS G B, MIRACLE D B, CHUANG C P, LIAW P K. Refractory high-entropy alloys [J]. Intermetallics, 2010, 18: 1758−1765.

[22] LIANG Song-mao, SCHMID-FETZER R. Evaluation of calphad approach and empirical rules on the phase stability of multi-principal element alloys [J]. Journal of Phase Equilibria and Diffusion, 2017, 38: 369−381.

[23] LI Rui-xuan, WANG Zhe, GUO Zhan-cheng, LIAW P K, ZHANG Tao, LI L, ZHANG Yong. Graded microstructures of Al−Li−Mg−Zn−Cu entropic alloys under supergravity [J]. Science China Materials, 2019, 62: 736−744.

[24] SHAO L, ZHANG T, LI L, ZHAO Y H, HUANG J F, LIAW P K, ZHANG Y. A low-cost lightweight entropic alloy with high strength [J]. Journal of Materials Engineering and Performance, 2018, 27: 6648−6656.

[25] ZHANG P, LI S X, ZHANG Z F. General relationship between strength and hardness [J]. Materials Science and Engineering: A, 2011, 529: 62−73.

[26] LI Rui, GAO Jia-cheng, FAN Ke. Study to microstructure and mechanical properties of Mg containing high entropy alloys [J]. Materials Science Forum, 2010, 650: 265−271.

[27] TUN K S, NAHATA A, VINCENT S, GUPTA M. Processing, microstructure and mechanical characterization of a new magnesium based multicomponent alloy [J]. Materials Today: Proceedings, 2020, 28: 1044−1047.

[28] SANCHEZ J M, VICARIO I, ALBIZURI J, GURAYA T, ACUÑA E M. Design, microstructure and mechanical properties of cast medium entropy aluminium alloys [J]. Scientific Reports, 2019, 9: 6792.

[29] SANCHEZ J M, PASCUAL A, VICARIO I, ALBIZURI J, GURAYA T, GALARRAGA H. Microstructure and phase formation of novel $Al_{80}Mg_5Sn_5Zn_5X_5$ light-weight complex concentrated aluminum alloys [J]. Metals, 2021, 11: 1944.

[30] PANDEY V K, SHADANGI Y, SHIVAM V, BASU J, CHATTOPADHYAY K, MAJUMDAR B, SARMA B N, MUKHOPADHYAY N K. Synthesis, characterization and thermal stability of nanocrystalline MgAlMnFeCu low-density high-entropy alloy [J]. Transactions of the Indian Institute of Metals, 2021, 74: 33−44.

[31] TUN K S, CHARADVA V, GUPTA M. Lightweight medium entropy magnesium alloy with exceptional compressive strength and ductility combination [J]. Journal of Materials Engineering and Performance, 2021, 30: 2422−2432.

[32] PARAMSOTHY M, CHAN J, KWOK R, GUPTA M. Al_2O_3 nanoparticle addition to commercial magnesium alloys:

Multiple beneficial effects [J]. Nanomaterials (Basel), 2012, 2: 147−162.

[33] CHEN Y L, HU Y H, HSIEH C A, YEH J W, CHEN S K. Competition between elements during mechanical alloying in an octonary multi-principal-element alloy system [J]. Journal of Alloys and Compounds, 2009, 481: 768−775.

[34] ZHAN Li-qiang, HOU Jia-bin, WANG Guo-feng, CHEN Yu-qing, LUO Shu-yi, KANG Qing-xin, LI Zhen-lun, XU Xun-hu. Study on mechanical alloying behavior and thermal stability of HfMoNbTaTi refractory high-entropy alloy [J]. Materials Characterization, 2023, 203: 113122.

[35] WANG Nai-ran, WANG Shou-ren, GOU Xiao-xiang, SHI Ze-cheng, LIN Jian-xiang, LIU Guo-qiang, WANG Yan. Alloying behavior and characterization of $(CoCrFeNiMn)_{90}$-M_{10} (M=Al, Hf) high-entropy materials fabricated by mechanical alloying [J]. Transactions of Nonferrous Metals Society of China, 2022, 32: 2253−2265.

[36] SINGH N, SHADANGI Y, MUKHOPADHYAY N K. Phase evolution and thermal stability of low-density MgAlSiCrFe high-entropy alloy processed through mechanical alloying [J]. Transactions of the Indian Institute of Metals, 2020, 73: 2377−2386.

[37] WU Shi-kai, PAN Ye, LU Jie, WANG Ning, DAI Wei-ji, LU Tao. Effect of the addition of Mg, Ti, Ni on the decoloration performance of AlCrFeMn high entropy alloy [J]. Journal of Materials Science & Technology, 2019, 35: 1629−1635.

[38] MAULIK O, KUMAR V. Synthesis of $AlFeCuCrMg_x$ (x=0, 0.5, 1, 1.7) alloy powders by mechanical alloying [J]. Materials Characterization, 2015, 110: 116−125.

[39] KHANCHANDANI H, SHARMA P, KUMAR R, MAULIK O, KUMAR V. Effect of sintering on phase evolution in $AlMgFeCuCrNi_{4.75}$ high entropy alloy [J]. Advanced Powder Technology, 2016, 27: 289−294.

[40] CAO P P, HUANG H L, JIANG S H, LIU X J, WANG H, WU Y, LU Z P. Microstructural stability and aging behavior of refractory high entropy alloys at intermediate temperatures [J]. Journal of Materials Science & Technology, 2022, 122: 243−254.

[41] YANG Teng-fei, XIA Song-qin, LIU Shi, WANG Chen-xu, LIU Shao-shuai, ZHANG Yong, XUE Jian-ming, YAN Sha, WANG Yu-gang. Effects of Al addition on microstructure and mechanical properties of $Al_xCoCrFeNi$ high-entropy alloy [J]. Materials Science and Engineering: A, 2015, 648: 15−22.

[42] HE Feng, WANG Zhi-jun, WU Qing-feng, LI Jun-jie, WANG Jin-cheng, LIU C T. Phase separation of metastable CoCrFeNi high entropy alloy at intermediate temperatures [J]. Scripta Materialia, 2017, 126: 15−19.

[43] XU X D, LIU P, GUO S, HIRATA A, FUJITA T, NIEH T G, LIU C T, CHEN M W. Nanoscale phase separation in a fcc-based $CoCrCuFeNiAl_{0.5}$ high-entropy alloy [J]. Acta Materialia, 2015, 84: 145−152.

[44] WANG Zhi-jun, HUANG Yun-hao, YANG Yong, WANG Jin-cheng, LIU C T. Atomic-size effect and solid solubility of multicomponent alloys [J]. Scripta Materialia, 2015, 94: 28−31.

[45] ZENG Xin, LI Fang-jie, ZHOU Xie, YAN Wei-zhi, LI Jiu-xiao, YANG Dong-ye, SHEN Qin, WANG Xiao-wei, LIU Min. The phase stability at intermediate-temperature and mechanical behavior of the dual-phase $AlCoCr0.5Fe_xNi_{2.5}$ high entropy alloys [J]. Materials Chemistry and Physics, 2023, 297: 127314.

[46] YANG X, CHEN S Y, COTTON J, ZHANG Y. Phase stability of low-density, multiprincipal component alloys containing aluminum, magnesium, and lithium [J]. JOM, 2014, 66: 2009−2020.

[47] GUO Sheng, NG Chun, LU Jian, LIU C T. Effect of valence electron concentration on stability of fcc or bcc phase in high entropy alloys [J]. Journal of Applied Physics, 2011, 109: 103505.

[48] BI Lin-xia, LI Xiao-na, HU Ying-lin, ZHANG Jun-yi, WANG Xiao, CAI Xue-cheng, SHEN Tong-de, LIU Ren-wei, WANG Qing, DONG Chuang, LIAW P K. Weak enthalpy-interaction-element-modulated NbMoTaW high-entropy alloy thin films [J]. Applied Surface Science, 2021, 565: 150462.

[49] CHEN Xing-qiu, NIU Hai-yang, LI Dian-zhong, LI Yi-yi. Modeling hardness of polycrystalline materials and bulk metallic glasses [J]. Intermetallics, 2011, 19: 1275−1281.

[50] FENG Xiang-zheng, PENG Jin-zhang, XU Zhong-fei, OUYANG Shi-liang. Investigations of mechanical and electronic properties for Al-based intermetallics with different Ti content [J]. The European Physical Journal Applied Physics, 2015, 69: 10203.

[51] ZHANG H, SHANG S L, WANG Y, SAENGDEEJING A, CHEN L Q, LIU Z K. First-principles calculations of the elastic, phonon and thermodynamic properties of $Al_{12}Mg_{17}$ [J]. Acta Materialia, 2010, 58: 4012−4018.

[52] LIU Tao, CHONG Xiao-yu, YU Wei, ZHOU Yun-xuan, HUANG Hai-guang, ZHOU Rong-feng, FENG Jing. Changes of alloying elements on elasticity and solid solution strengthening of α-Ti alloys: A comprehensive high-throughput first-principles calculations [J]. Rare Metals, 2022, 41: 2719−2731.

[53] ZHOU Yun-xuan, TIAN Wen-jun, DONG Quan, WANG Hai-lian, ZHANG Jie, TAN Jun. First-principles calculations to investigate mechanical, electronic, optical, and thermodynamic properties of Zr-based ternary compounds [J]. Journal of Materials Research and Technology, 2023, 23: 1417−1434.

[54] HE Yu, XIE You-qing, PENG Kun, LIU Xin-bi. Electronic structures and properties of pure vanadium [J]. Transactions of Nonferrous Metals Society of China, 1999, 19: 446−450.

[55] SONG Yu, ZHAN Song-tao, NIE Bao-hua, QI Hai-ying, LIU Fang-jun, FAN Tou-wen, CHEN Dong-chu. First- principles investigations on structural stability, elastic properties and electronic structure of $Mg_{32}(Al,Zn)_{49}$ phase and $MgZn_2$ phase [J]. Crystals, 2022, 12: 683.

[56] ZHOU Yun-xuan, YU Wei, CHONG Xiao-yu, WEI Yan, HU Chang-yi, ZHANG Ai-min, FENG Jing. Rapid screening of alloy elements to improve the elastic properties of dilute Pt-based alloys: High-throughput first-principles calculations and modeling [J]. Journal of Applied Physics, 2020, 128: 235103.

Al−Li−Mg−Ti−M (M=Zn，Zr，V)轻质高熵合金的显微组织、相稳定性和力学性能

董 权[1]，李 萌[1]，张宇飞[1]，张 静[1,2]

1. 重庆大学 材料科学与工程学院，重庆 400044；
2. 重庆大学 国家镁合金材料工程技术研究中心，重庆 400044

摘 要：研究了 Al−Li−Mg−Ti−M(M=Zn，Zr，V)轻质高熵合金(LW-HEAs)的显微组织演变、相稳定性和力学性能。根据 HEA 的热力学设计标准设计了 $Al_{20}Li_{20}Mg_{10}Ti_{40}Zn_{10}$ (#Zn)、$Al_{20}Li_{20}Mg_{10}Ti_{30}Zr_{20}$ (#Zr)和 $Al_{20}Li_{20}Mg_{10}Ti_{30}V_{20}$ (#V) 3 种成分的 LW-HEAs，并通过机械合金化和冷压烧结相结合的方法制备了这 3 种合金。研究了合金成分及烧结温度对 LW-HEAs 显微组织和力学性能的影响。结果表明，球磨后的 Al−Li−Mg−Ti−M (M=Zn，Zr，V) LW-HEAs 分别形成了以 HCP 型固溶体为主要相、双 HCP 型固溶体相和 BCC 相的简单结构。经过冷压烧结后，#Zn 和#V 合金发生了明显的相变；而含有双 HCP 相的#Zr 合金在热处理过程中的相稳定性最好。在 BCC 相固溶强化和 β-$AlTi_3$ 沉淀强化的共同作用下，#V-750 ℃合金的硬度和比强度最高，分别达到 HV 595.2 和 625 MPa·cm^3/g。#Zr-650 ℃、#Zr-750 ℃、和#Zn-650 ℃合金有望具有优异的塑性。

关键词：轻质高熵合金；机械合金化；显微组织演变；相稳定性；比强度；塑性

(Edited by Wei-ping CHEN)